Fast Prediction of Hydrodynamic Load of Floating Horizontal Axis Tidal Turbine with Variable Speed Control under Surging Motion with Free Surface

Siyuan Chen[1], Shuqi Wang[1,*], Ruizhang Huang[1], Weichao Shi[2], Fengmei Jing[3]

(1. *School of Naval Architecture and Ocean Engineering, Jiangsu University of Science and Technology, Zhenjiang 212003, China*)

(2. *Department of Naval Architecture, Ocean and Marine Engineering, University of Strathclyde, Glasgow, G40LZ, U.K.*)

(3. *School of Mechanical Engineering, Beijing Institute of Petrochemical Technology, Beijing 102617, China*)

Abstract: For floating HATT[1] with variable speed control, a numerical model based on CFD[2] method is proposed to predict the surge force. Compared with the hydrodynamic load of the HATT under the same condition but with fixed speed control, the variable speed control can effectively improve the power coefficient of the HATT. When the surge period is 1.5 s and the surge amplitude is *D*/8, the average power coefficient increases by 36.36%. But the load fluctuation in terms of the axial load and power coefficients are significantly larger than those with fixed speed control. Based on the hydrodynamic load decomposition model of the HATT with fixed speed rotation and surging motion and the variation law of damping coefficient, the hydrodynamic load prediction method of the HATT with variable speed rotation and surging motion is established. By comparing with the CFD results, it is evidenced that this prediction method can effectively predict the axial load and power coefficients of the HATT. The research findings can provide a reference for the rapid prediction of the hydrodynamic load of the HATT during the actual operation of the floating tidal power station.

Key words: Horizontal axis tidal turbine; Hydrodynamic characteristics; Rotation speed control; Prediction method; Surging motion

Nomenclature

Symbols	Descriptions	Symbols	Descriptions
U	Inflow velocity, m/s	ξ_S	Surging displacement, m
ω_T	Turbine angular velocity, rad/s	A_S	Surge amplitude, m
D	Turbine diameter, m	ω_S	Surge frequency, rad/s
R	Turbine radius, m	T_S	Surge period, s
ρ	Water density, kg/m3	N	Number of blades
U_r	Relative inflow velocity, m/s	C_{Fx}	Axial force coefficient
U_S	Surge velocity, m/s	C_P	Power coefficient
λ	Tip speed ratio	n	Normalized damping coefficients
λ_{opt}	Optimal tip speed ratio	m	Normalized added mass coefficients
F_X	Axial force, N	$\bar{u}$	Dimensionless surging velocity
T_X	Axial torque, Nm	$\bar{a}$	Dimensionless surging acceleration

1. Introduction

According to BP World Energy Outlook 2018, the development of renewable energy will grow rapidly in the future with 33% expected by 2040 (Dudley, 2018). Ocean energy is a type of renewable energy that contains abundant untapped resources. With 70% of the earth's surface covered by the ocean, tidal current energy is one kind of ocean energy (Draper et al., 2014; Liu et al., 2022], which could provide 50-180GWh of electricity per year. Such great potential in the past decades has attracted scholars from all over the world (Chen et al., 2018). With continuous research and development, various tidal energy devices have been prototyped and trialled (Liu et al.,

[1] HATT: horizontal axis tidal turbine
[2] CFD: Computational fluid dynamics

2018). According to the different working modes of tidal turbines, they can be divided into horizontal and vertical axis tidal turbines (Zhang et al., 2013). Compared with the vertical axis turbine, the advantages of the HATT are clear, including simple structure, better efficiency, self-starting and stable rotation, etc. (Li, 2008). According to Corsatea surveys, 76% of investment in the tidal current energy industry is used to develop HATT (Corsatea et al., 2013).

Recently, floating platforms are explored, which are demonstrated to be suitable for complex seabed terrain, large range of water depth, good use of surface water flow and easy installation and maintenance (Jing et al., 2013; Wang et al., 2020). However, in the real ocean environment, due to wind, wave and turbulence, the floating platform is subjected to complex motions which complicate the hydrodynamic load of HATT. Furthermore, the presence of waves in the tidal current field can lead to the following two problems: 1, the waves generate orbital velocity mixing into the tidal current field and hence lead to spatial-temporal velocity fluctuation, which results in load fluctuation and compromises the energy conversion efficiency and the power quality; 2, for floating tidal energy devices, the waves excite the platform to have significant motion together with fast rotating turbines. This leads to further load fluctuation and impacts power quality and output. Both phenomena contribute to the fatigue load of the turbine structure and shorten the operational life of tidal energy devices. Therefore, it is vital to discuss the hydrodynamic performance of a floating HATT under the wave-current interaction.

Recently, many researchers have studied the hydrodynamic load of a HATT under wave-current conditions either through model experiments or numerical simulation. For example, Henriques et al. (2014) carried out a three-bladed HATT model test with a diameter of 0.5m in the high-speed circulating water flume, and the thrust and power output of the HATT under two different regular wave conditions were measured. The results show that the regular wave has little effect on the time mean value of the thrust and power coefficient of the HATT, but the instantaneous value has obvious periodic fluctuation, and the fluctuation frequency is the same as the wave frequency. Ma et al. (2017) conducted experiments on a two-bladed HATT with a diameter of 0.7m in the towing tank. The axial load and power output of a HATT were measured under the conditions of blade tip-immersion depth of 0.15m and 0.55m, respectively. The experimental results show that when the turbine is close to the water surface, the power efficiency will increase due to the influence of waves, and the influence of waves on the axial load of the HATT will gradually decrease with the increase of blade tip-immersion depth. Guo et al. (2018) studied the thrust and torque of a HATT with a diameter of 0.8 m in a towing tank with a towing velocity of 0.68 m/s. The experimental results show that the fluctuation amplitudes of thrust and torque reached up to 50% of their average values when the wave period is 1.6 s and wave height is 0.14 m. Draycott et al. (2019) conducted experiments on a three-bladed HATT with a diameter of 1.2 m at the FloWave circular, and the thrust and power output under the conditions of regular waves were measured. Results demonstrated that the wave-induced fluctuations of the thrust and power output had increased with the wave amplitude, but it had decreased with wave frequency. Rodrigo et al. (2018) conducted experiments on the same HATT model, and the thrust and power in oblique currents and wave conditions were measured. Results demonstrated that waves affect the means and standard deviation of HATT thrust and power, but off-axis waves are associated with lower thrust loads than head-on waves. Shi et al. (2019) conducted a test on the leading-edge undulated tidal turbine in a towing tank facility under the conditions of regular waves and irregular waves. Results revealed that the leading-edge undulated turbine has a stable hydrodynamic performance over a combined range of current speeds and waves. Zhang et al. (2023)conducted a test on a three-bladed HATT with a diameter of 0.2 m. The experimental results demonstrated that the power spectrum under wave conditions is almost a superposition of current and additional components, including wave frequency, rotation frequency, and their mixing frequency.

In terms of numerical methods, BEM[3] and CFD methods are mainly used in the study of hydrodynamic loads of HATT. Some researchers have improved the BEM method and used it to study the hydrodynamic load of a HATT under wave-current conditions (Scarlett et al., 2019, 2020; El-Shahat et al., 2020, 2022). Although BEM method has been developed and applied to the hydrodynamic load calculation of a HATT under wave-current conditions, this method has limitations, for example, it does not solve the blade grids and can not give detailed flow around the rotor. However, CFD method based on Reynolds-averaged Numerical Simulation can effectively overcome these limitations. From the literature, there are few studies on the hydrodynamic load of a HATT under wave-current conditions based on CFD method. Jia et al. (2020) used Star-CCM+ software to study the hydrodynamic performance of the coupled motion between the HATT and the carrier platform. The results showed that: the wave height and wavelength have significant impacts on the pitch, heave and surge of the floating platform and the HATT, and the pitch, heave and surge increase with the increase of wave amplitude. Tian et al. (2020) applied the CFD method to analyze the hydrodynamic performance of a HATT under wave-current conditions. The findings proved that both the time mean value and the fluctuation amplitude of the HATT torque were increasing with the increase of wave height. Huang et al. (2022) applied the CFD method to investigate the effects of heave motion on the performance of a floating counter-rotating turbine under wave-current interaction. The simulation results show that the mean power and thrust coefficients are reduced by about 9% and 5%, respectively. Peng et al. (2022) used the CFD method to investigate the HATT performance under free surface condition and with surge motion. The simulation results show that augmenting the surge amplitude and frequency increases the time-averaged and fluctuation of the power and thrust coefficient.

In summary, most existing studies considered the effect of waves on the flow field, but did not take into account the influence of waves on the motion of the floating platform, that is, the HATT rotates around a fixed axis in a wave-current field. In fact, the wave causes the platform to move with six degrees of freedom, and the HATT fixed on the floating body will rotate and move with the platform in six degrees of freedom. Prior studies (Wang et al., 2019, 2021) had reported that the frequency and amplitude of the surging motion can affect the hydrodynamic load and power output of the HATT with fixed speed rotation and surging motion, but the effect of the varying rotational speed was not considered. During the actual operation, some turbines use variable speed control which will be adversely affected by this. It is necessary to analyze the influence of the floating platform motion on a variable speed controlled turbine.

Therefore, this paper proposes a speed control law based on the floating platform movement to achieve the purpose of improving the output power of the HATT. Then, based on the previous study (Wang et al., 2021), a numerical simulation method of variable speed rotation and surging movement of a HATT under free surface conditions is established, and the hydrodynamic loads of the HATT under different surge periods and amplitudes is analyzed. Finally, by using the hydrodynamic load decomposition model and the variation law of damping coefficient under the fixed speed rotation and surging motion of the HATT, a fast hydrodynamic load prediction method under the variable speed rotation and surging motion is established. The findings can provide a reference for the rapid prediction of the hydrodynamic load of the HATT during the actual operation of the floating tidal power station, and provides a basis for the research of the motion response of the floating platform and the design of the HATT control system.

2. CFD Numerical Simulation

2.1 CFD Numerical Methods

In our previous work (Wang et al., 2021), a numerical calculation method for the hydrodynamics load of the

[3] BEM: Blade-Element Momentum

HATT with constant speed rotation and surging motion under the condition of free surface has been established, and the validity of the numerical calculation method is verified by comparing it with the experimental results. The turbine diameter and blade number are 0.7 m and 2, respectively. Two domains are established: the background domain and the rotation domain. The distances of the turbine rotation plane from the inlet boundary and the outlet boundary of the background domain are 5D and 15D respectively, and the distance of the turbine rotation axis from the bottom and the side of the background domain are 5D. The distance between the rotating center of HATT and the top side of the background domain is set as 2.5D. This paper studies the hydrodynamic load characteristics and power characteristics of the HATT with variable speed rotation and surging motion ($U_S=A_S\omega_S\cos(\omega_S t)$) under the condition of the free surface. As far as the numerical simulation method is concerned, the main difference between the numerical method proposed in this paper and the numerical method established in our previous work is the setting of the rotational speed. In our previous work, the rotational speed is constant, while the rotational speed of the HATT in this paper is variable. Therefore, on the basis of the numerical calculation method established in the literature (Wang et al., 2021), the speed is controlled to realize the numerical simulation of the variable speed rotation and surging motion of the HATT. The mesh model used in this paper is consistent with that described in literature (Wang et al., 2021), as shown in Fig. 1. The target size and minimum size of turbine surface are set as 0.002 m and 0.0005 m in Fig.2c. As shown in Fig.2c, the height of the HATT surface mesh of the first layer height is 0.0005 m, the stretching ratio is 1.1, the number of boundary layers is 10, and the y+ ranges in 0.7~48. In Fig.1d, the free surface mesh encryption area is enlarged near the HATT in order to capture the deformation of the free-surface. The number of cells in the whole computing domain is more than 4.5 million.

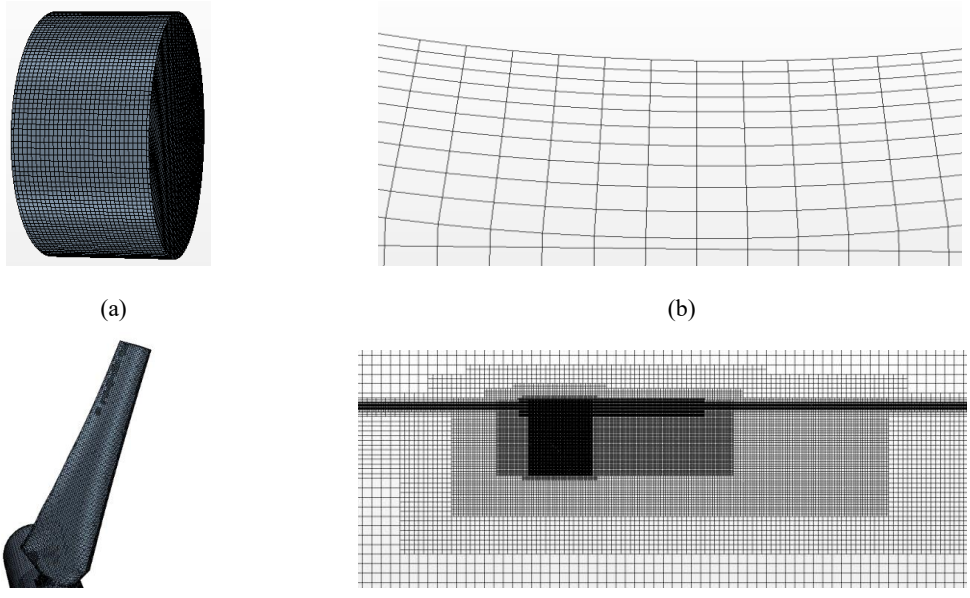

(a) (b)

(c) (e)

Fig.1 Mesh model. (a) Rotation domain mesh; (b) Boundary layer mesh; (c) Blade surface mesh; (e) XOZ plane mesh.

Rotation and surging motion are realized by sliding grid and overlapping grid respectively. The motion model of rotation and surging is established, and then the surging velocity and variable rotation speed are given in the rotation domain. Next, this paper set the atmosphere as the standard pressure and the direction of gravitational acceleration (-Y). The inlet boundary (Inlet) is set as the velocity entry, and the uniform flow velocity U (1 m/s) and turbulence parameters are given. The outlet boundary is set as the pressure outlet， and the hydrostatic pressure is given. According to the blade tip-immersion depth, the volume fractions of water and air at the inlet and outlet are given. In addition, the bottom and sides of the computational domain are set as free slip walls. The top of the computational domain is set as an open pressure boundary, the relative pressure is set as 0, and the volume fraction

of water and air are 0 and 1 respectively. The HATT surface is the non-slip wall. The background and rotating domains are connected by an overlapping grid. The boundary conditions are set as shown in Fig.3. The turbulence model is SST model.

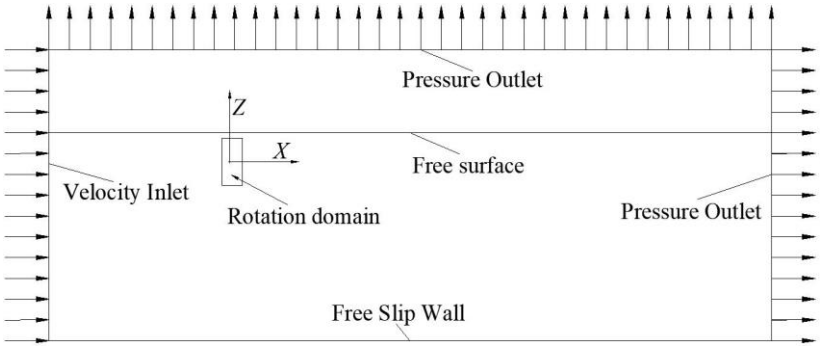

Fig.2 Schematic diagram of boundary conditions

2.2 Rotating speed control model

According to the previous research results, the power coefficient of the HATT reaches the maximum when the tip speed ratio is about 5.5 under the condition of uniform open flow, that is, the optimal tip speed ratio is about 5.5. Due to the existence of the surging motion, the relative inflow velocity of the HATT changes. If the rotational speed is constant, the speed ratio will change all the time during the surging motion. Considering the influence of the surging motion on the relative inflow velocity of the turbine, the rotational speed is controlled to make the HATT always operate near the optimal tip speed ratio, to improve the power coefficient of the HATT under the condition of surging motion. According to the law of surging motion, the surge velocity of the HATT can be obtained as:

$$U_S = A_S \omega_S \cos(\omega_S t) \tag{1}$$

Without considering the influence of the induced velocity, the relative inflow velocity of the HATT can be expressed as

$$U_r = U - A_S \omega_S \cos(\omega_S t) \tag{2}$$

Set the optimal tip speed ratio λ_{opt} to 5.5, then the corresponding control rotation speed is

$$\omega_T = \frac{\lambda_{opt}\left[U - A_S \omega_S \cos(\omega_S t)\right]}{R} \tag{3}$$

Based on Eq. (3), a user-defined function about the rotational speed is established in commercial software Star-CCM+ to realize the control of the rotating speed of the HATT. Since the rotating speed of the HATT changes at all times and the magnitude of the change is related to the surge amplitude and frequency, if a constant time step is used, it is not conducive to the convergence of the calculation results. Therefore, according to the rotational speed, a field function about the time step is established to achieve the purpose of rotating the HATT by 2° at each time step.

3. Results and analysis

For the load and performance of the HATT, the axial load and output power are more concerned. So the two dimensionless parameters are defined as follows.

$$C_{Fx} = \frac{F_X}{\frac{1}{2}\rho U^2 \pi R^2} \tag{4}$$

$$C_P = \frac{T_X \omega_T}{\frac{1}{2}\rho U^3 \pi R^2} \tag{5}$$

$$\lambda = \frac{\omega_T R}{U} \tag{6}$$

The diameter of the prototype turbine is 9 m, the tidal current speed is about 3.5 m/s, and the wave period is from 4 s to 7 s. The diameter of the HATT model in numerical simulation is 0.7 m. Based on the Froude's similarity law, the inflow velocity during numerical calculation is 1 m/s, and the wave period is around 1.1 s -1.9 s. It is assumed that the period of the surging motion is the same as that of the wave.

3.1. Influence of surge period on hydrodynamic performance

By selecting the surge amplitude as $D/16$, the blade tip immersion water depth as $D/8$, and the incoming flow velocity as 1m/s, the time history curves of the axial load and power coefficients under three different surge periods (1.1s, 1.5s, and 1.9s) were calculated, and the results are given in Fig. 3. In the figure, -F represents the calculation result when the rotation speed is fixed, and -V represents the calculation result when the rotation speed changes according to Eq. (3).

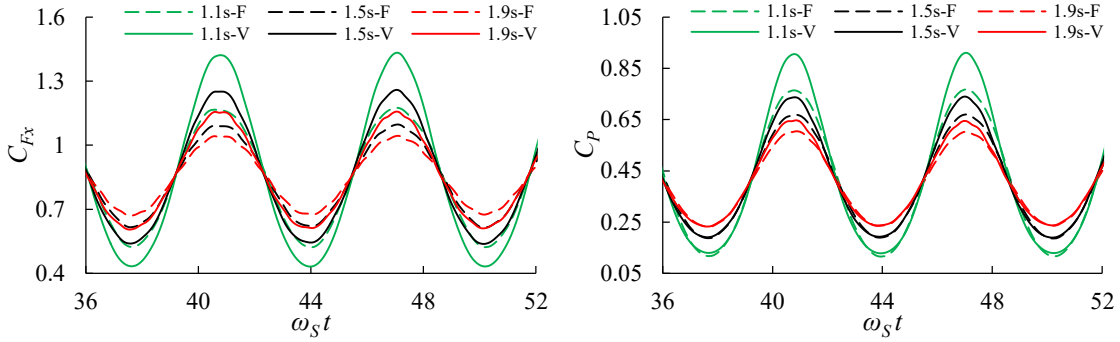

Fig.3 Time history curves of the hydrodynamic load under different surge periods. (a) Axial load coefficient; (b) Power coefficient.

It can be seen from Fig. 3 that whether the rotational speed is fixed or the rotational speed is changed according to Eq. (3), both the axial load and power coefficients have obvious periodic fluctuations. The fluctuation period is consistent with the surge period, and the fluctuation amplitude increases with the decrease of the surge period. It can be explained as follows: for fixed rotational speed motion, the relative inflow velocity at the rotational plane of the HATT changes periodically with the surging motion, and the smaller the period, the greater the variation of the relative inflow velocity; for variable rotational speed motion, except that the relative inflow velocity at the rotating plane of the HATT changes with the surging motion, the rotation speed of the HATT also changes periodically with the surging motion, and the smaller the period, the larger the variation range of the relative inflow velocity and rotation speed. Moreover, the fluctuation amplitude and average value of the axial load and power coefficients under the condition of variable rotational speed are larger than those under the condition of fixed rotational speed in Fig. 3. Especially for the power coefficient, the calculation results of the variable rotational speed motion are larger than the calculation results of the fixed rotational speed motion, and the smaller the period, the more obvious the difference. Compared with the average power coefficient under fixed rotational speed, the average power coefficient under varying rotational speed during the surge period of 1.9s, 1.5s and 1.1s increases by 5.98%, 9.77% and 19.00%, respectively. The main reason is that the HATT always works at the optimal tip speed ratio during the variable rotational speed motion, which improves the power output of the HATT. Therefore, making the HATT always works at the optimal tip speed ratio can effectively improve the power generation of the floating tidal current power station.

3.2. Influence of surge amplitude on hydrodynamic performance

The surge period, the blade tip immersion water depth**,** and the incoming flow velocity are set as 1.5s, *D*/8, and 1 m/s, respectively. Then the hydrodynamic loads under different surge amplitudes (*D* /32, *D* /16, 3 *D* /32, *D* /8) were calculated. The time history curves of the axial load and power coefficients are shown in Fig. 4, where -F indicates the calculation result when the rotational speed is fixed and -V indicates the calculation result when the rotational speed is varied according to Eq. (3).

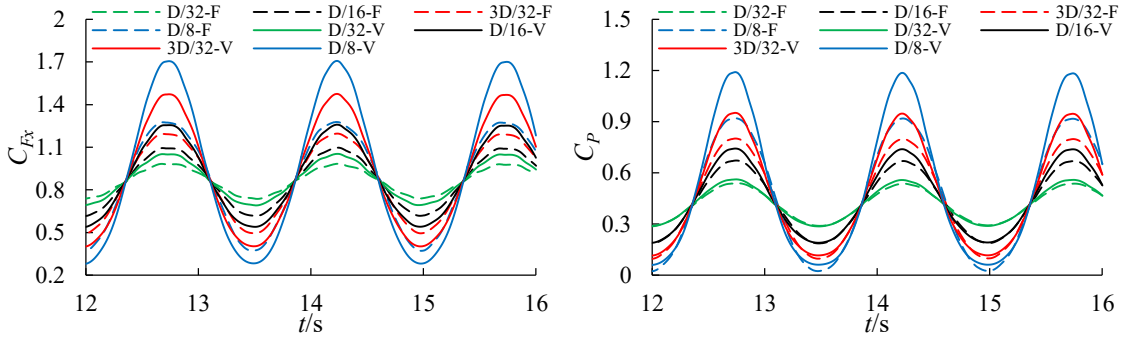

Fig.4 Time history curves of the hydrodynamic load under different surge amplitudes. (a) Axial load coefficient; (b) Power coefficient.

It can be found from the Fig. 4 that 1) with the increase of the surge amplitude, the fluctuation amplitude of the axial load and power coefficients gradually increases, but the fluctuation period is consistent with the surge period; 2) the fluctuation amplitude and average value of axial load and power coefficients under the condition of variable rotational speed are greater than those under the condition of fixed rotational speed; 3) compared with the power coefficient under fixed rotational speed, the larger the surge amplitude, the more obvious the increase of power coefficient under variable rotational speed motion. Compared with the average power coefficient under fixed rotational speed, the average power coefficient under varying rotational speed during the surge amplitude of *D*/32, *D*/16, 3*D*/32 and *D*/8 increases by 2.63%, 9.77%, 21.15% and 36.36%, respectively.The reason is similar to the influence of the surge period on the axial load and power coefficients, that is, under the same surge period, the amplitude of the surging motion determines the variation range of the relative inflow velocity and rotational speed. The larger the surge amplitude is, the larger the variation range of relative inflow velocity and rotational speed is, resulting in the larger the fluctuation amplitude of the hydrodynamic load of the HATT.

3.3. Influence of rotational speed on hydrodynamic performance

To obtain the influence of the rotational speed on the hydrodynamic load of the HATT and provide data support for the hydrodynamic load prediction method when the rotational speed is variable. This paper set the surge period as 1.5s, the surge amplitude as *D*/16, the immersion depth of the blade tip as *D*/8, and the incoming flow velocity as 1m/s. 11 different fixed rotational speeds are selected for numerical calculation, and the variation law of hydrodynamic load at different fixed rotational speeds is obtained in Fig. 5. The numbers in the legend indicate the tip speed ratios. It can be seen from Fig. 5 that under different fixed rotational speeds, the axial load and power coefficients fluctuate periodically with the surging motion. The fluctuation period is consistent with the surge period, and the fluctuation amplitude gradually increases with the increase of rotational speed. The main reason is that the faster the rotational speed, the greater the relative velocity of the airfoil of the HATT blade section, resulting in a greater magnitude of the hydrodynamic load change caused by the same surge velocity change. The variation law of the average value of the axial load and power coefficients with the rotation speed is consistent with that of axial load and power coefficients when only rotating, that is, with the increase of the rotation speed, the average value of axial load coefficient gradually increases, but the average value of the power coefficient first increases and then decreases. As far as the power coefficient is concerned, there is an optimal speed ratio, that is,

the corresponding tip speed ratio when the power coefficient achieves maximum is about 5.5.

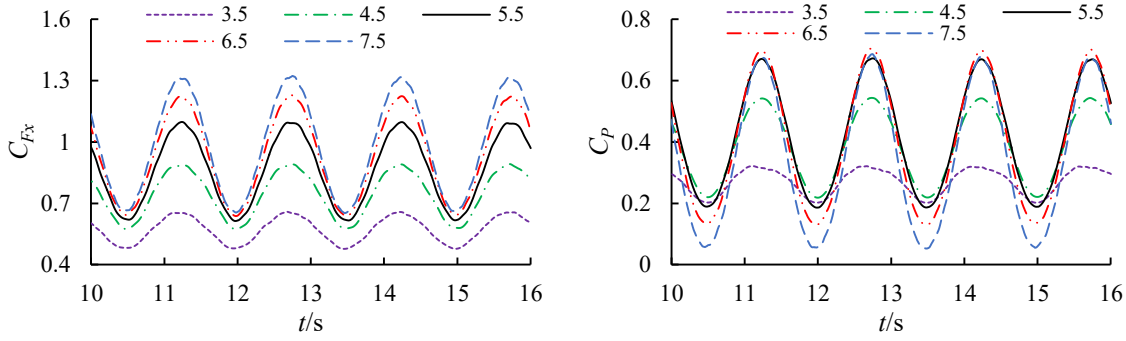

(a) (b)

Fig.5 Time history curves of the hydrodynamic load under different tip speed ratios. (a) Axial load coefficient; (b) Power coefficient.

4. Hydrodynamic load prediction method

4.1. Decomposition analysis of hydrodynamic load at a fixed rotating speed

4.1.1. Hydrodynamic load decomposition model

According to the analysis of the calculation results in Section 3 and the hydrodynamic load characteristics of the HATT, the decomposition model of the axial load and power coefficients is established as follows.

$$\begin{aligned} C_{Fx} &= C_{Fx}^{0} + \sum_{i_0=1}^{m_0} C_{Fx}^{i_0} \sin\left(i_0 N\omega_T t + \psi_{FxT}^{i_0}\right) \\ &+ \sum_{j=1}^{n_1}\left(C_{Fx1}^{0j} + \sum_{i_1=1}^{m_1} C_{Fx1}^{i_1 j} \sin\left(i_1 N\omega_T t + \psi_{FxT1}^{i_1}\right)\right)\sin\left(j\omega_S t\right) \\ &+ \sum_{k=1}^{n_2}\left(C_{Fx2}^{0k} + \sum_{i_2=1}^{m_2} C_{Fx2}^{i_2 k} \sin\left(i_2 N\omega_T t + \psi_{FxT2}^{i_2}\right)\right)\cos\left(k\omega_S t\right) \end{aligned} \tag{7}$$

$$\begin{aligned} C_{P} &= C_{P}^{0} + \sum_{i_0=1}^{m_0} C_{P}^{i_0} \sin\left(i_0 N\omega_T t + \psi_{PT}^{i_0}\right) \\ &+ \sum_{j=1}^{n_1}\left(C_{P1}^{0j} + \sum_{i_1=1}^{m_1} C_{P1}^{i_1 j} \sin\left(i_1 N\omega_T t + \psi_{PT1}^{i_1}\right)\right)\sin\left(j\omega_S t\right) \\ &+ \sum_{k=1}^{n_2}\left(C_{P2}^{0k} + \sum_{i_2=1}^{m_2} C_{P2}^{i_2 k} \sin\left(i_2 N\omega_T t + \psi_{PT2}^{i_2}\right)\right)\cos\left(k\omega_S t\right) \end{aligned} \tag{8}$$

The correlation coefficients in Eqs. (7-8) can be obtained by fitting the axial load and power coefficients time history curve based on the least square method. By analyzing and comparing the correlation coefficients, the following expressions can be obtained by ignoring the parts with small influence.

$$C_Z = C_Z^0 + C_{Z2}^{01}\cos\left(\omega_S t\right) \tag{9}$$

$$C_P = C_P^0 + C_{P2}^{01}\cos\left(\omega_S t\right) + C_{P2}^{02}\cos\left(2\omega_S t\right) \tag{10}$$

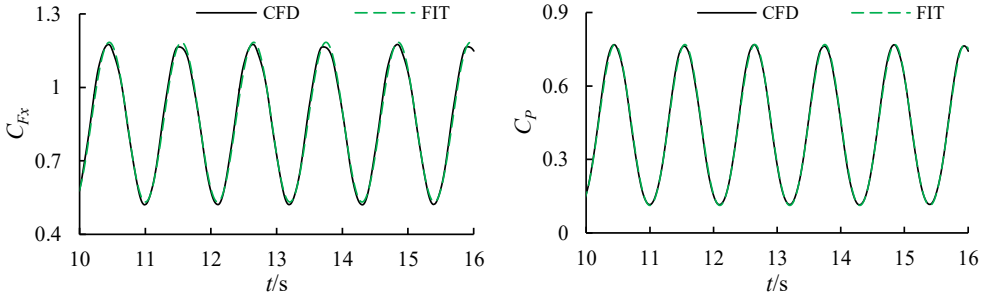

(a)

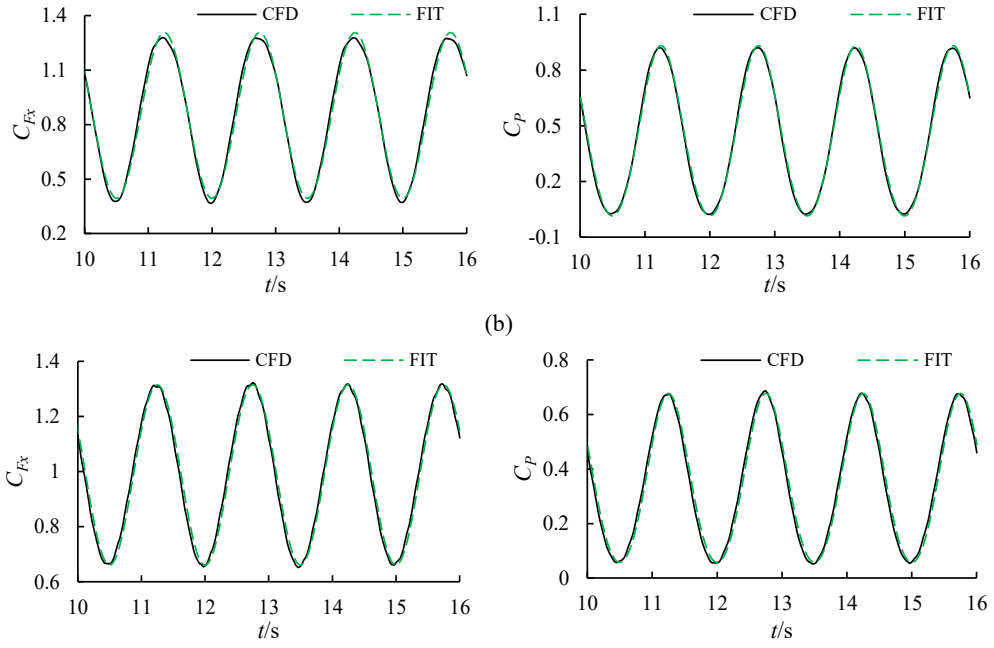

Fig.6 Comparison of calculated values between formula and CFD. (a) H=D/8, A_S =D/16, T_S =1.1s，λ=5.5; (b) H=D/8, A_S =D/8, T_S =1.5s，λ=5.5; (c) H=D/8, A_S =D/16, T_S =1.5s，λ=7.5.

The comparison curve of calculation value obtained by Eqs. (9-10) and CFD are given in Fig.6. The calculation value obtained by Eqs. (9-10) basically keeps the same with the calculated value obtained by CFD. Therefore, Eqs. (9-10) can reflect the hydrodynamic characteristics of HATT with surging motion under free surface conditions. According to the law of surging motion, the dimensionless surge velocity is defined as shown in Eq. (11). Thus, Eqs. (9-10) can be written as Eqs. (12-13), which ignores the effects of additional mass and divides hydrodynamic loads into two parts: the hydrodynamic load when only rotating is considered, and the damping force related to the surge velocity. In Eqs. (12-13), the damping coefficient of the axial load coefficient is stable during the surging motion, but the damping coefficient of the power coefficient changes periodically based on the surge frequency.

$$\overline{u} = \frac{A_S \omega_S \cos(\omega_S t)}{U} \tag{11}$$

$$C_{Fx} = C_{Fx}^0 + C_{Fx2}^{01} \cos(\omega_S t) = C_{Fx}^0 + n_{FxS} \overline{u}_S \tag{12}$$

$$\begin{aligned} C_P &= C_P^0 + C_{P2}^{01} \cos(\omega_S t) + C_{P2}^{02} \cos(2\omega_S t) \\ &= C_P^0 + \left[n_{PS}^0 + n_{PS}^1 \cos(\omega_S t) \right] \overline{u}_S - C_P^{02} \\ &= C_P^{0'} + \left[n_{PS}^0 + n_{PS}^1 \cos(\omega_S t) \right] \overline{u}_S \end{aligned} \tag{13}$$

4.1.2. The effect of the surge period on the fitting coefficient

For the time history curves of the axial load and power coefficients under different surge periods, the correlation coefficients in Eqs. (12-13) can be obtained by fitting with the least square method and given in Tables 1-2. As can be seen from Tables 1-2, C_{Fx}^0 and $C_P^{0'}$ are stable, that is, the change of the surge period has little effect on the time mean of the axial load and power coefficients. For the axial load coefficient, the damping coefficient is stable under different surge periods, that is, the axial load coefficient has a linear relationship with the dimensionless surge velocity. For the power coefficient, the average value of the damping coefficient is stable under different surge periods, but its fluctuation amplitude increases linearly with the increase of the surge frequency in Fig. 7, that is, the damping coefficient of the power coefficient fluctuates with the surging motion, and the

fluctuation amplitude increases linearly with the increase of the surge frequency.

Table 1 C_{Fx} correlation coefficients

T_S (s)	C_{Fx}^0	n_{FxS}
1.1	0.858	-1.304
1.3	0.860	-1.308
1.5	0.861	-1.301
1.7	0.861	-1.287
1.9	0.861	-1.272

Table 2 C_P correlation coefficients

T_S (s)	$C_P^{0'}$	n_{PS}^0	n_{PS}^1
1.1	0.416	-1.315	0.100
1.3	0.414	-1.320	0.092
1.5	0.413	-1.322	0.090
1.7	0.410	-1.298	0.080
1.9	0.409	-1.282	0.076

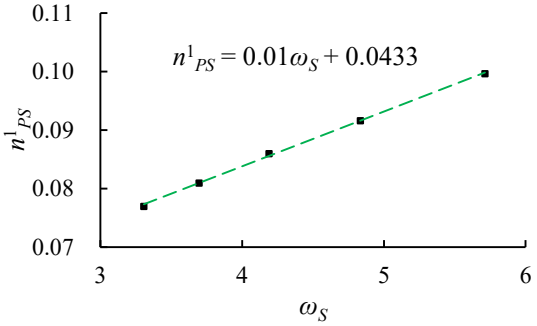

Fig. 7 Variation law of n_{PS}^1 with surge frequency

4.1.3. The effect of the surge amplitude on the fitting coefficient

Based on Eqs. (12-13), the axial load and power coefficients at different surge amplitudes are fitted by using the least squares method, and the correlation coefficients in Eqs. (12-13) can be obtained, and the detailed results are given in Tables 3-4.

Table 3 C_{Fx} correlation coefficients

A_S	C_{Fx}^0	n_{FxS}
D/32	0.863	-1.311
D/16	0.865	-1.301
3D/16	0.870	-1.277
D/8	0.877	-1.245

Table 4 C_P correlation coefficients

A_S	$C_P^{0'}$	n_{PS}^0	n_{PS}^1
D/32	0.410	-1.337	0.047
D/16	0.413	-1.322	0.090
3D/16	0.418	-1.290	0.115
D/8	0.425	-1.248	0.131

As can be seen from Tables 3-4, C_{Fx}^0 and $C_P^{0'}$ keep stable, that is, the changes in the surge amplitude also have little effect on the time mean of the axial load and power coefficients. For the axial load coefficient, the

damping coefficient is stable under different surge amplitudes, and the difference is within 5%, that is, the axial load coefficient is also basically linear with the dimensionless surge velocity. For the power coefficient, the average value of the damping coefficient is also basically stable under different surge amplitudes, but its fluctuation amplitude increases linearly with the increase of the surge amplitude in Fig. 8, that is, the damping coefficient of the power coefficient fluctuates with the surging motion, and the fluctuation amplitude increases approximately linearly with the increase of surge amplitude.

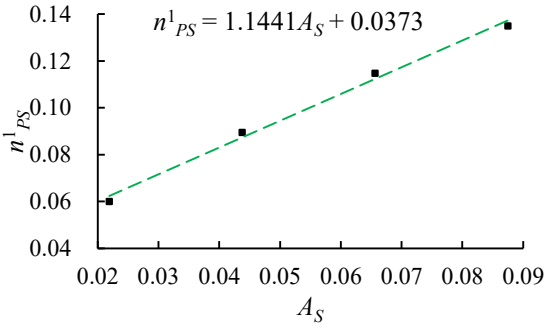

Fig. 8 Variation law of n^1_{PS} with surge amplitude

4.1.4. The effect of the tip speed ratio on the fitted coefficient

Based on Eqs. (12-13), the axial load and power coefficients at different tip speed ratios are fitted using the least squares method, and the correlation coefficients can be obtained, and they are listed in Tables 5-6.

Table 5 C_{Fx} correlation coefficients

λ	C^0_{Fx}	n_{FxS}
3	0.484	-0.444
3.5	0.571	-0.411
4	0.661	-0.614
4.5	0.743	-0.847
5	0.809	-1.094
5.5	0.861	-1.301
6	0.902	-1.454
6.5	0.934	-1.576
7	0.961	-1.679
7.5	0.987	-1.783
8	1.008	-1.867

Table 6 C_P correlation coefficients

λ	$C^{0'}_P$	n^0_{PS}	n^1_{PS}
3	0.188	-0.102	-0.051
3.5	0.269	-0.311	-0.118
4	0.332	-0.577	-0.094
4.5	0.386	-0.885	-0.059
5	0.409	-1.118	0.006
5.5	0.421	-1.322	0.090
6	0.415	-1.449	0.134
6.5	0.401	-1.546	0.168
7	0.380	-1.621	0.193
7.5	0.347	-1.691	0.217

8	0.308	-1.745	0.237

As can be seen from Tables 5-6, with the increase of the tip speed ratio, C_{Fx}^{0} gradually increases (as shown in the Fig. 9(a)). $C_{P}^{0'}$ first increases and then decreases (as shown in the Fig. 9(b)), and a maximum value is obtained when the tip speed ratio is about 5.5. It is consistent with the change of the axial load and power coefficients with the tip speed ratio when the HATT rotates at only a fixed rotation speed, and the value is the same. For the axial load coefficient, except that the tip speed ratio is 3, the absolute value of the damping coefficient increases as a quadratic function with the increase of the tip speed ratio (as shown in Fig. 9(c)). For the power coefficient, the average value of the absolute value of the damping coefficient also increases in a quadratic function with the increase of the tip speed ratio (as shown in Fig. 9(d)), but its fluctuation amplitude has no obvious law with the increase of the tip speed ratio.

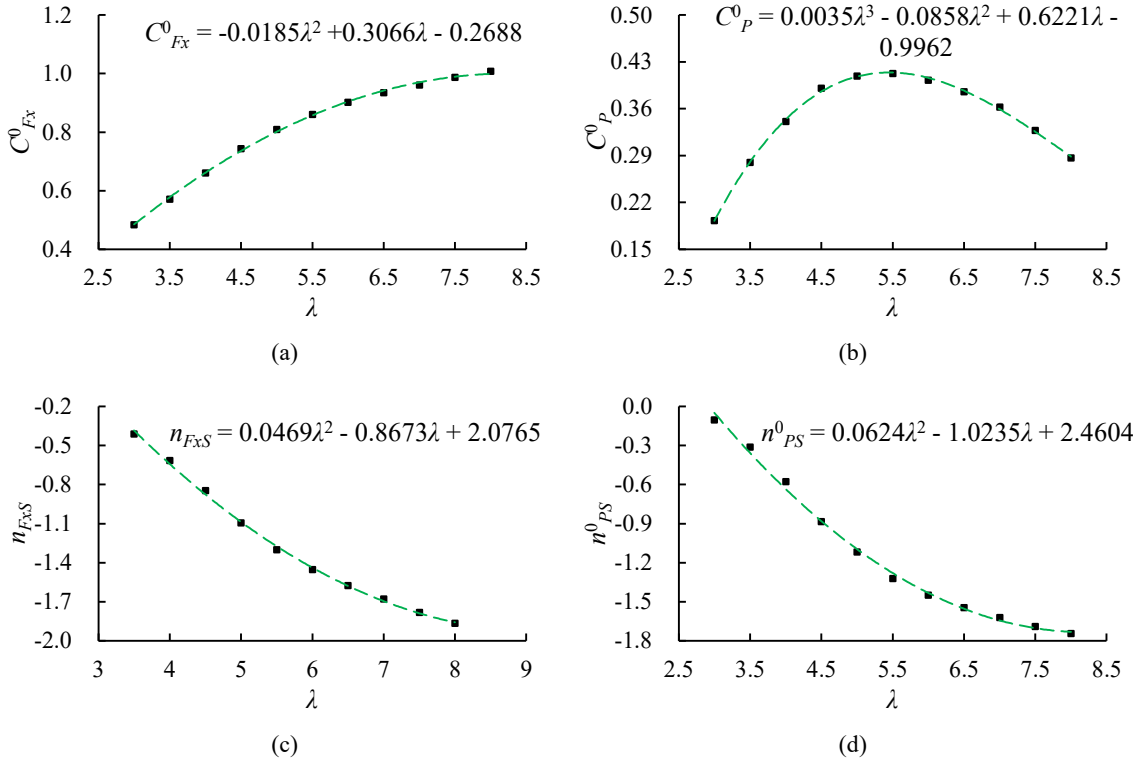

Fig. 9 Variation law of correlation coefficients with tip speed ratio. (a) C_{Fx}^{0}; (b) $C_{P}^{0'}$; (c) n_{FxS}; (d) n_{PS}^{0}.

4.2. Prediction method of hydrodynamic load with variable rotational speed

4.2.1. Prediction model of hydrodynamic load

It can be seen from the analysis in Section 4.1 that when the HATT rotates at a fixed speed, C_{Fx}^{0}, $C_{P}^{0'}$, n_{FxS} and n_{PS}^{0} are basically independent of surging motion, but only a function of the rotation speed; n_{PS}^{1} is a function of the surge frequency, surge amplitude and rotation speed. Therefore, according to the hydrodynamic load decomposition model and the obtained correlation coefficient under the conditions of fixed speed rotation and surging motion of the HATT, the fast prediction model of axial load and power coefficients under the conditions of variable speed rotation and surging motion of the HATT can be obtained, as shown below.

$$C_{Fx} = C_{Fx}^{0}(\lambda) + n_{FxS}(\lambda)\bar{u}_S \tag{14}$$

$$C_P = C_P^{0'}(\lambda) + \left[n_{PS}^0(\lambda) + n_{PS}^1(A_S, \omega_S, \lambda)\cos(\omega_S t) \right] \bar{u} \tag{15}$$

According to the analysis in Section 4.2, if the relationship between C_{Fx}^0 and tip speed ratio, n_{FxS} and tip speed ratio, n_{PS}^0 and tip speed ratio is fitted with quadratic function, and the relationship between $C_P^{0'}$ and tip speed ratio is fitted with cubic function, Eqs. (14-15) can be written as follows.

$$C_{Fx} = -0.0185\lambda^2 + 0.3066\lambda - 0.2688 + \left(0.0469\lambda^2 - 0.8673\lambda + 2.0765\right)\bar{u}_S \tag{16}$$

$$\begin{aligned} C_P = {} & 0.0035\lambda^3 - 0.0858\lambda^2 + 0.6221\lambda - 0.9962 \\ & + \left[0.0624\lambda^2 - 1.0235\lambda + 2.4604\right]\bar{u} \\ & + \left[n_{PS}^1(\lambda) + 1.1508\left(A_S - D/16\right) + 0.01\left(\omega_S - 4.18879\right) \right]\cos(\omega_S t)\bar{u} \end{aligned} \tag{17}$$

In Eq. (17), since the change law of $n_{PS}^1(\lambda)$ with tip speed ratio is not obvious, interpolation is based on radial basis function. The form of the basis function is shown in the following formula.

$$f_i(x) = e^{-p\left(\frac{x - x_i}{r}\right)^2} \qquad (i = 1-11), \tag{18}$$

where $r = r_{11} - r_1$, and p is the parameter with a value ranging from 1–1000, the value is 10 in this study.

$$y_j = \sum_{i=1}^{11} C_i f_i(x_j) \qquad (j = 1-11), \tag{19}$$

where C_i is the unknown coefficient. Once the value of C_i from the known data points is obtained, the relationship between x and y can be defined.

$$y = \sum_{i=1}^{11} C_i f_i(x) \tag{20}$$

According to the value of $n_{PS}^1(\lambda)$ in Table 6, the value of C_i about $n_{PS}^1(\lambda)$ can be obtained in Table 7.

Table 7. Numerical table of C_i

	C_1	C_2	C_3	C_4	C_5	C_6	C_7	C_8	C_9	C_{10}	C_{11}
$n_{PS}^1(\lambda)$	-28.928	168.264	-497.536	990.373	-1477.112	1730.136	-1616.494	1193.474	-668.151	256.748	-51.325

Based on Eqs. (16-17) and (20), as well as Table 7, the axial load and power coefficients of the HATT can be quickly calculated under the conditions of rotation at different rotational speeds and surging motion.

4.2.2. Verification of hydrodynamic load prediction model

Based on the prediction model of the axial load and power coefficients established in Subsection 4.3.1, the axial load and power coefficients under the condition of variable rotational speed can be calculated and the comparisons of the CFD calculation results are given in Fig. 10.

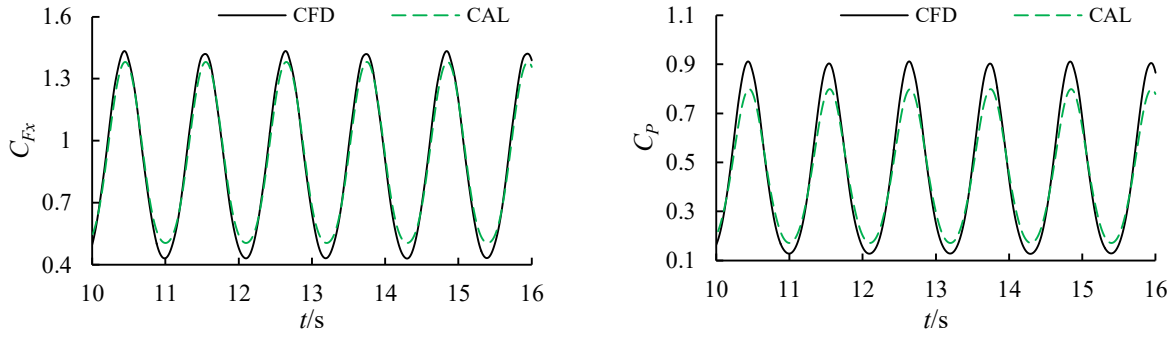

(a)

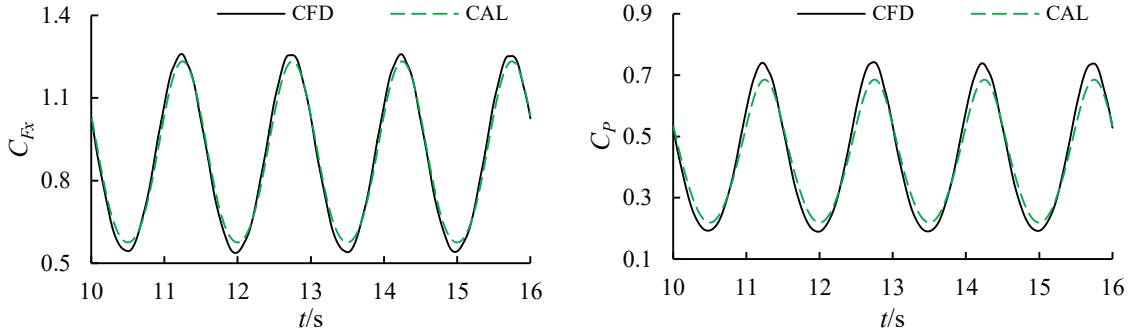

(b)

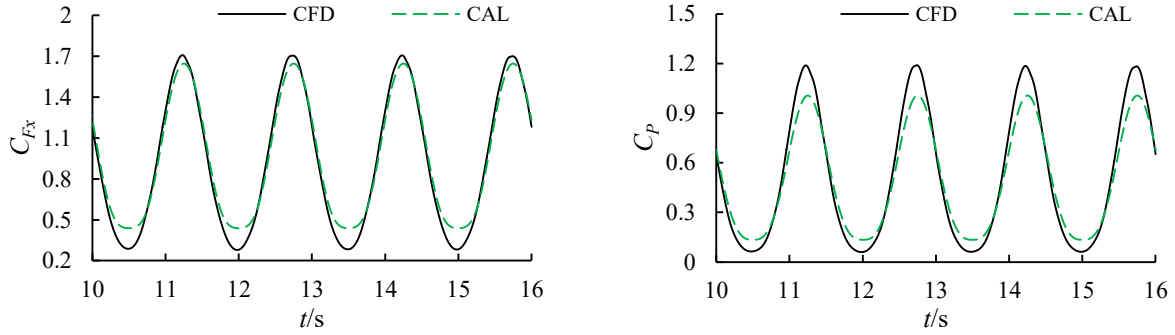

(c)

Fig. 10 Comparison between calculated values of prediction model and CFD. (a) A_S =D/16, T_S =1.1s; (b) A_S =D/16, T_S =1.5s; (c) A_S =D/8, T_S =1.5s.

As can be seen from Fig. 10, the calculated values based on the prediction model are basically consistent with the CFD calculations, but differ greatly around the peak point. By analyzing Figs. 10(a) and 10(b), the smaller the surge period, the greater the difference near the peak point. In Figs. 10(b) and 10(c), the larger the surge amplitude, the greater the difference near the peak point. There are two main reasons: 1) on the one hand, it is caused by the surging motion, the smaller the surge period or the larger the surge amplitude, the greater the surging motion acceleration of the HATT, while the hydrodynamic load prediction model does not consider the influence of surging motion acceleration; 2) on the other hand, it is the influence of the change of the HATT rotating speed, the smaller the surge period or the larger the surge amplitude, the larger the variation range of the HATT rotating speed, and the larger the rotating acceleration, while the prediction model does not consider the influence of the rotating acceleration. To further clarify the main reason for the difference near the peak point, the axial load and power coefficients of the HATT with only variable speed rotating motion are calculated based on the established CFD method. On this basis, considering the influence of the surging motion on the axial load and power coefficients, that is, considering the surge damping coefficient, the axial load and power coefficients of the HATT with variable speed rotation and surging motion can be obtained, and the expression is as follows.

$$C_{Fx} = C^{0}_{Fx\_CFD} + \left(0.0469\lambda^2 - 0.8673\lambda + 2.0765\right)\bar{u}_S \tag{21}$$

$$\begin{aligned} C_P = {} & C^{0}_{P\_CFD} + \left[0.0624\lambda^2 - 1.0235\lambda + 2.4604\right]\bar{u} \\ & + \left[n^{1}_{PS}(\lambda) + 1.1508\left(A_S - D/16\right) + 0.01\left(\omega_S - 4.18879\right)\right]\cos\left(\omega_S t\right)\bar{u} \end{aligned} \tag{22}$$

The comparative curve of the axial load and power coefficients under different calculation methods is shown in Fig. 11, where CFD represents the calculation results based on CFD, CAL1 represents the calculation results based on Eqs. (16-17), and CAL2 represents calculations based on Eqs. (21-22).

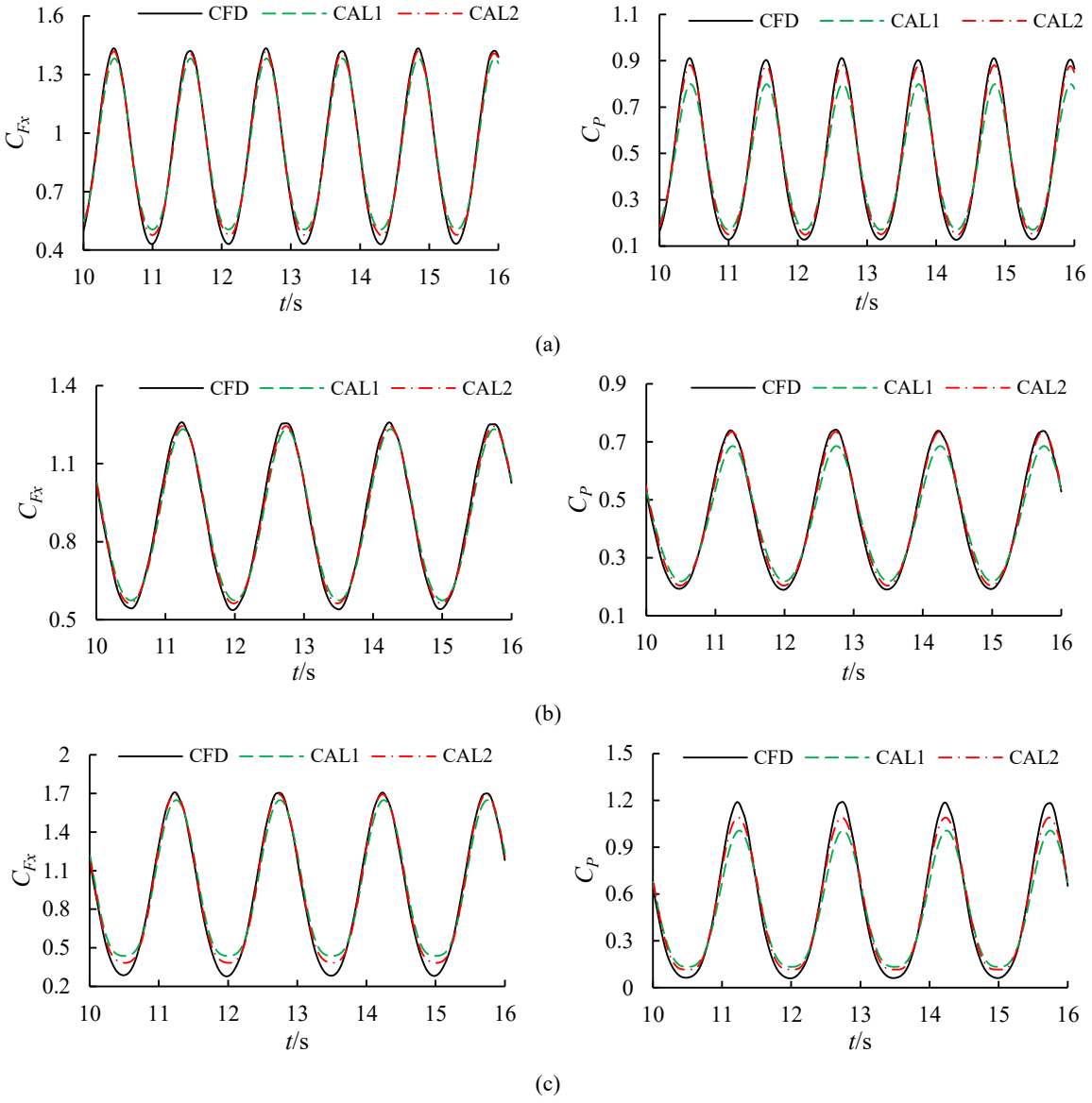

Fig. 11 Comparison between calculated values of prediction model and CFD. (a) A_S =D/16, T_S =1.1s; (b) A_S =D/16, T_S =1.5s; (c) A_S =D/8, T_S =1.5s.

In Fig. 11, the calculation results based on Eqs. (21-22) are significantly closer to CFD calculation results than those based on Eqs. (16-17), and their errors are generated due to the neglect of the effects of the additional mass coefficient and the higher-order terms of the surge frequency. The results indicate that the axial load and power coefficients are related to the rotation speed and the change speed of the rotation speed when the HATT only rotates because of the influence of the induced velocity. The faster the rotation speed changes, the greater the induced velocity, resulting in the greater difference in the axial load and power coefficients between the variable rotation speed and the fixed rotation speed of the HATT (as shown in Fig. 12, CAL represents the calculation result based

on the cubic polynomial fitting formula in Fig. 8 (b)). Fig. 11 also shows that the influence of surging motion on the axial load and power coefficients of HATT has little relationship with the change speed of rotating speed. Therefore, when the HATT is rotating and surging at the same time, the hydrodynamic load of the HATT can be obtained by adding the influence of surging motion to the hydrodynamic load of HATT rotating motion only (as shown in Eqs. (21-22)), and can also be approximately estimated based on the prediction model (as shown in Eqs. (16-17)).

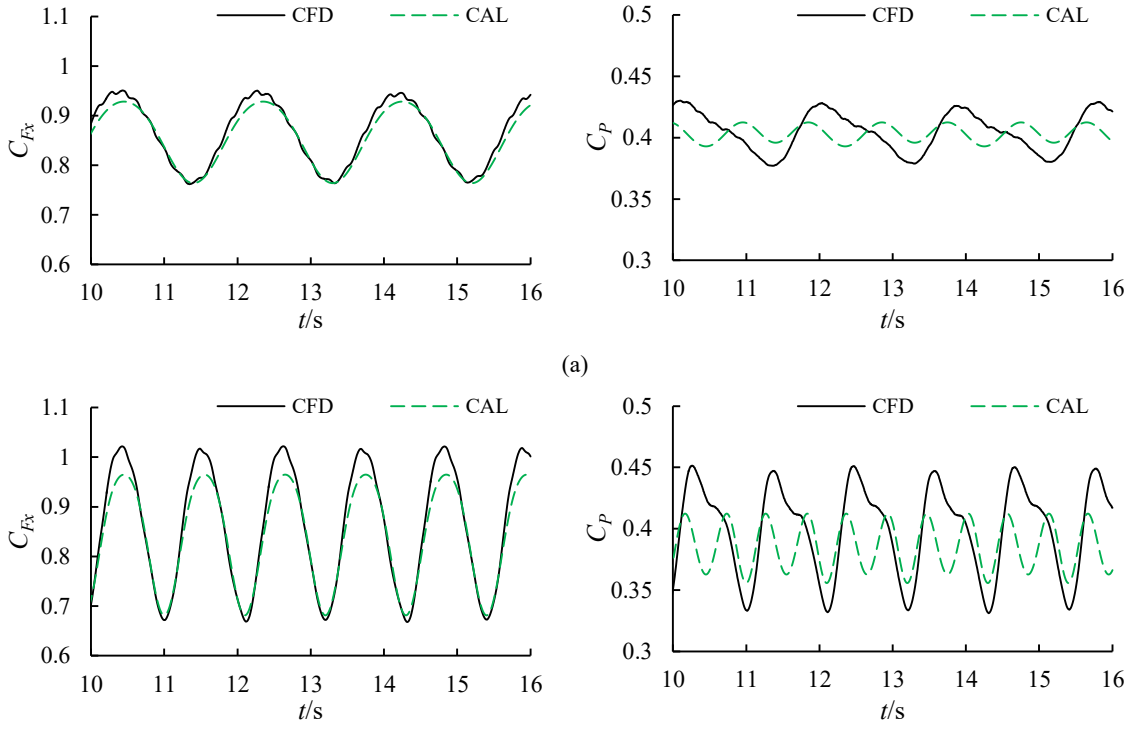

Fig. 12 Comparison between calculated values of fitting formula and CFD under variable speed rotation only. (a) $\omega_T = \dfrac{\lambda_{opt}\left[U - A_S\omega_S\cos(\omega_S t)\right]}{R}$: A_S =D/16, T_S =1.9s; (b) $\omega_S = \dfrac{\lambda_{opt}\left[U - A_S\omega_S\cos(\omega_S t)\right]}{R}$: A_S =D/16, T_S =1.1s.

5. Conclusion

In this study, a numerical simulation method for the HATT with variable speed rotation and surging motion under the condition of the free surface is proposed, and the axial load and power coefficients under different surge periods and surge amplitudes are obtained to compare with those under fixed rotation speed. On this basis, the hydrodynamic load under fixed speed rotation and surge motion is decomposed into the hydrodynamic load when only rotating and the damping force related to surge speed are considered. Based on the least square method, the variation law of damping coefficient under different surge periods, surge amplitudes and tip speed ratios is obtained. Finally, a hydrodynamic load prediction method of the HATT under variable speed rotation and surging motion is proposed to compare with the CFD results. The research findings can be concluded as follows.

1) There are obvious periodic fluctuations in the instantaneous values of axial load and power coefficients under variable speed rotation and surging motion, and the fluctuation amplitude increases with the increase of surge amplitude, surge frequency and rotation speed;

2) The speed control model proposed in this paper can effectively improve the power coefficient of the HATT with surging motion, and the average power coefficient under varying rotational speed during the surge period is 1.5 s and the surge amplitude is D/8 increases by 36.36%;

3) The damping coefficient of axial load and power coefficients changes slightly with the surging motion

parameters, that is, it remains stable with the increase of surge frequency and surge amplitude, but changes significantly with rotation speed;

4) The influence of rotating speed on the axial load and power coefficients of HATT is closely related to the change speed of rotating speed, but the influence of surging motion on the axial load and power coefficients is not related to the change speed of rotating speed;

5) The proposed hydrodynamic load prediction method can effectively predict the axial load and power coefficients of the HATT during variable speed rotation and surging motion.

Acknowledgement

This work was supported by the National Natural Science Foundation of China (No. U1706227, 52071348, and 51979129); the Innovation Group Project of Southern Marine Science and Engineering Guangdong Laboratory (Zhuhai) (No.311021013). Natural Science Research of Jiangsu Higher Education Institutions of China （22KJA130001）

References

Corsatea T.D., Magagna D., Overview of European innovation activities in marine energy technology, JRC Science and Policy Reports. 2013.

Chen H., Tang T., Aït-Ahmed N., et al, Attraction, challenge and current status of marine current energy, IEEE Access. 6 (2018) 12665-12685.

De Jesus Henriques T.A., Tedds S.C., Botsari A., et al, The effects of wave–current interaction on the performance of a model horizontal axis tidal turbine, International Journal of Marine Energy. 8 (2014) 17-35.

Draper S., Adcock T.A.A., Borthwick A.G.L., et al, Estimate of the tidal stream power resource of the Pentland Firth, Renewable Energy. 63 (2014) 650-657.

Dudley B. BP statistical review of world energy. BP statistical review, London, UK, accessed Aug, 6(2018) 00116.

Draycott S., Payne G., Steynor J., et al, An experimental investigation into non-linear wave loading on horizontal axis tidal turbines, Journal of Fluids and Structures. 84 (2019) 199-217.

El-Shahat S.A., Li G.J., Fu L., Linear and non-linear wave theories coupled with a modified BEM model for quantifying dynamic loads of a tidal stream turbine, Ocean Engineering. 243 (2022) 110334.

El-Shahat S.A., Fu L., Li G.J., Dynamic loading characterization of a horizontal axis tidal current turbine, Ocean Engineering. 211 (2020) 107561.

Guo X., Yang J., Gao Z., et al, The surface wave effects on the performance and the loading of a tidal turbine, Ocean Engineering. 156 (2018) 120-134.

Huang B., Zhou B.W., Wang L., te al, The effects of heave motion on the performance of a floating counter-rotating type tidal turbine under wave-current interaction, Energy Conversion and Management. 252 (2022) 115093.

Jing F., Mehmood N., Zhang L., et al, Optimal selection of floating platform for tidal current power station, Research Journal of Applied Sciences, Engineering and Technology. 6 (2013) 1116-1121.

Jia X.B., Zhang X.W., Chen P., The influence law of wave condition on tidal turbine and carrier platform, Water Resources and Power. 38(06) (2020) 162-164.

Li Y.W., Marine Energy Development. Beijing, Ocean Press. 2008.03.

Liu Y.X., Ma C.L., Jiang B., Development and the environmental impact analysis of tidal current energy turbines in China, IOP Conference Series: Earth and Environmental Science. 2018, 121(4).

Liu S.Y., Zhang J.S., Sun K., et al, Performance and near-wake characteristics of a bidirectional horizontal-axis tidal turbine, Applied Ocean Research. 125 (2022) 103246.

Ma W.J., Jing F.M., Wang S.Q., et al, The experimental study on the performance of tidal current turbine under the combined action of wave and current, China shipbuilding.58(02) (2017) 189-198.

Martinez R., Payne G.S., Bruce T., The effects of oblique waves and currents on the loadings and performance of tidal turbines, Ocean Engineering. 164 (2018) 55-64.

Peng B., Zhang Y.Q., Zheng Y., et al, The effects of surge motion on the dynamics and wake characteristics of a floating tidal stream turbine under free surface condition, Energy Conversion and Management. 266 (2022) 115816.

Shi W., Atlar M., Nirman R., et al, Effect of waves on the leading-edge undulated tidal turbines, Renewable Energy. 131 (2019) 435-447.

Scarlett G.T., Sellar B., Bremer T.V.D., et al, Unsteady hydrodynamics of a full-scale tidal turbine operating in large wave conditions, Renewable Energy. 143 (2019) 199-213.

Scarlett G.T., Viola I.M., Unsteady hydrodynamics of tidal turbine blades, Renewable Energy. 146 (2020) 843-855.

Tian W.L., Ni X.W., Mao Z.Y., et al, Influence of surface waves on the hydrodynamic performance of a horizontal axis ocean current turbine, Renewable Energy. 158 (2020) 37-48.

Wang S.Q., Cui J., Ye R.C., et al, Study of the Hydrodynamic Performance Prediction Method for a Horizontal-Axis Tidal Current Turbine with Coupled Rotation and Surging Motion, Renewable Energy. 135 (2019) 313-325.

Wang S.M., et al. A review of the development of international trend energy utilization technology, Ship engineering. 42(S1) (2020) 23-28.

Wang S.Q., Zhang Y., Xie Y.Y., et al, The effects of surge motion on hydrodynamics characteristics of horizontal-axis tidal current turbine under free surface condition, Renewable Energy. 170 (2021):773-784.

Zhang L., Li X.Z., Geng J., et al, Tidal Current Energy Update 2013, Advances in New and Renewable Energy. 1(1) (2013) 53-68.

Zhang Z., Zhang Y.Q., Zheng Y., et al, Power fluctuation and wake characteristics of tidal stream turbine subjected to wave and current interaction, Energy. 264 (2023) 126185.

Appendix: Using Π -Buckingham theorem to obtain dimensionless numbers

The axial load coefficient (C_{Fx}) of HATT is the dimensionless load coefficient along the direction of rotation axis. Power coefficient (C_P) is a parameter that represents the ability of the HATT to absorb tidal current kinetic energy. These coefficients are based on F_X and P which are a functions of following variables

$$\{F_X, P\} = f\left(H, R, \omega_T, U, U_S, \omega_S, \rho, \mu, g, t, N\right), \tag{1}$$

where $U_S = A_S\omega_S \cos(\omega_S t)$ is the surge velocity. All other variable follow the manuscript nomenclature.

Using the Π -Buckingham theorem and selecting R, U and ρ as basic physical quantities, we get

$$\{C_{Fx}, C_P\} = f^*\left(H^*, \lambda, U_S{}^*, \omega_S{}^*, \mathrm{Re}, \mathrm{Fr}, t^*, N\right), \tag{2}$$

$$C_{Fx} = \frac{F_X}{\frac{1}{2}\rho U^2 \pi R^2} \tag{3}$$

$$C_P = \frac{T_X \omega_T}{\frac{1}{2}\rho U^3 \pi R^2} \tag{4}$$

$$H^* = \frac{H}{R} \quad , \tag{5}$$

$$\lambda = \frac{\omega_T R}{U} \quad , \tag{6}$$

$$H^* = \frac{H}{R} \quad , \tag{7}$$

$$\lambda = \frac{\omega_T R}{U} \quad , \tag{8}$$

$$U_S{}^* = \frac{U_S}{U} . \tag{9}$$

The other dimensionless variables were obtained manipulating variables of the original set

$$\omega_S{}^* = \frac{\omega_S R}{U}\lambda^{-1} = \frac{\omega_S}{\omega_T} \quad , \tag{10}$$

$$\mathrm{Re} = \frac{\omega_T R}{U}\frac{\rho U R}{\mu} = \frac{\rho \omega_T R^2}{\mu} \quad , \tag{11}$$

$$\mathrm{Fr} = \frac{U}{\sqrt{gR}} \quad , \tag{12}$$

$$t^* = \frac{Ut}{R}\lambda = \omega_T t \, , \tag{13}$$

Where Re and Fr and the well-know Reynolds and Froude numbers.